Chemical routes to materials

Abrupt change from moderate positive to colossal negative thermal expansion caused by imidazolate composite formation

Sanja Burazer[1] , Lukáš Horák[1] , Yaroslav Filinchuk[2] , Radovan Černý[3,*] , and Jasminka Popović[4,*]

[1] *Department of Condensed Matter Physics, Charles University, Ke Karlovu 5, 121 16, Prague 2, Czech Republic*

[2] *Institute of Condensed Matter and Nanosciences, Université Catholique de Louvain, Place L. Pasteur 1, 1348 Louvain-la-Neuve, Belgium*

[3] *Laboratory of Crystallography, DQMP, University of Geneva, Quai Ernest-Ansermet 24, CH-1211 Geneva, Switzerland*

[4] *Laboratory for Synthesis and Crystallography of Functional Materials, Division for Materials Physics, Ruđer Bošković Institute, Bijenička 54, 10000 Zagreb, Croatia*

ABSTRACT

This work describes temperature-induced crystallization processes and reaction mechanisms occurring in the borohydride-imidazolate system. In the course of thermal evolution, crystal structures of two novel bimetallic imidazolates $AMnIm_3$ (A = Na, K) were solved using synchrotron radiation powder diffraction data. Both the alkali metal cation and the Mn cations exhibit distorted octahedral coordination while each imidazolate is surrounded by two alkali metal and two manganese atoms. Extensive study of the thermal expansion behaviour revealed that the expansion of the bimetallic imidazolates does not proceed uniformly over the entire temperature range but rather abruptly changes from a colossal negative to a moderate positive volume expansion. Such behaviour is caused by the coherent intergrowth of the coexisting phases which form a composite, a positive lattice mismatch and a tensile strain during the coexistence of $NaMIm_3$ (M = Mg and Mn) and NaIm or HT-NaIm. Such coherent coalescence of two materials opens the possibility for targeted design of zero thermal expansion materials.

Handling Editor: Catalin Croitoru.

Address correspondence to E-mail: Radovan.Cerny@unige.ch; jpopovic@irb.hr
E-mail Addresses: Sanja.Burazer@irb.hr; horak@karlov.mff.cuni.cz; Yaroslav.Filinchuk@uclouvain.be

Springer

GRAPHICAL ABSTRACT

Crystal structures of $AMnIm_3$ (A = Na, K) were determined. Coherently intergrown $NaMIm_3/NaIm$ (M = Mg, Mn) present colossal negative thermal expansion.
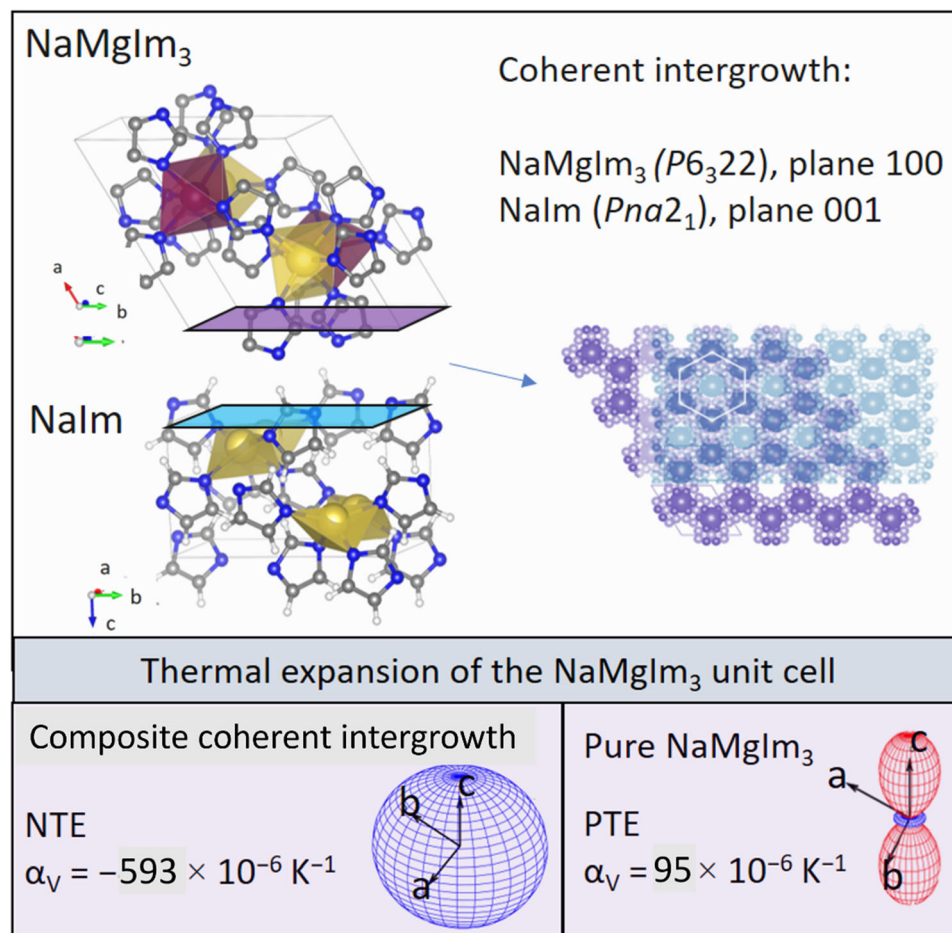
Introduction

Typically, many materials exhibit positive thermal expansion (PTE). Nowadays, the materials science community is intrigued by the uncommon phenomenon that occurs in some types of materials, causing them to contract when heated, i.e. to exhibit a negative thermal expansion (NTE). Such thermal behaviour enables fabrication of composites materials with a tailored coefficient of thermal expansion,

namely, zero expansion [1]. Zero expansion could prevent performance deterioration or even failure of devices caused by large differences in expansion coefficients [2]. In some typical NTE materials, such as ZrW_2O_8 [3], $Cd(CN)_2$ [4] and ScF_3 [5] with linear coefficients ranging from $\alpha = -14 \times 10^{-6}$ K^{-1} for ScF_3 [6] to $\alpha = -34 \times 10^{-6}$ K^{-1} for $Cd(CN)_2$, contraction upon temperature increase has been reported [7]. For molecular materials, the NTE behaviour usually depends on many factors, including transverse vibrational modes, geometric flexibility, host-

guest interaction, spin states, molecular packing arrangements, and molecular configurations [8]. Various metal–organic frameworks (MOFs) show NTE values of -27×10^{-6} K$^{-1} \leq \alpha \leq -11 \times 10^{-6}$ K^{-1} [9]. To emphasize the differences from typical framework behaviour, the term "colossal" is used for coefficients $\geq 100 \times 10^{-6}$ K^{-1} [10–12]. As an example, the perovskite PbVO$_3$ exhibits $\alpha = -590 \times 10^{-6}$ K^{-1} albeit in a short temperature interval of only 30 K [13]. Polycrystalline materials, especially those prepared by high energy ball milling, contain numerous microstructural imperfections. Numerous properties, such as microstructural, optical, electrical and magnetic are typically strongly temperature dependent but in some cases, the thermal expansion behaviour can also be extremely temperature dependent in the sense that a material exhibiting PTE in one temperature range can abruptly change its thermal expansion behaviour and end up with NTE in another temperature range [14–19]. One such example is the cyanide-bridged Fe^{III}–Co^{III} complex; a compound that exhibits an immense volumetric coefficient of thermal expansion of 1498×10^{-6} K^{-1} (between 180 and 240 K) followed by a negative volumetric expansion coefficient of -489×10^{-6} K^{-1} in the temperature range of 300–350 K [20]. The formation of the two-phase composite with PTE and NTE materials is an effective way to obtain (near) zero-thermal expansion materials, especially needed and utilized in the fields of mechanics and aerospace [21–33]. While intrinsic properties, such as electronic, ferroelectric or magnetic behaviour sensitive to microstructure, are considered as cause of thermal expansion, the influence of surface and interface on thermal expansion still needs more research [1, 34–36].

In an endless sea of metal organic frameworks (MOFs), experiencing explosive growth due to their ample chemical versatility, exceptional porosity and a wide range of potential applications including gas storage, separation, and catalysis, zeolitic imidazolate frameworks (ZIFs) are extremely popular [37]. They contain a combination of tetrahedral nodes which incorporate electronic properties of the transition metal ions and bent linkers that mimic the structural features of zeolites [38]. While various metal centres have been vastly studied, alkali metals have been left out of focus possibly due to the fact that NaIm, KIm and LiIm do not form porous frameworks, yet their dense and hypercoordinated structures have been observed [39, 40]. Nevertheless, our recent work has shown that the high-temperature polymorph of NaIm is capable of forming a porous structure [41]. On the other hand, magnesium imidazolate has been considered as a promising complexing agent due to the nature of the magnesium ion and its coordination chemistry. The studies carried out by Safin and collaborators revealed that the freshly synthesized MgIm$_2$ is amorphous but annealing at higher temperatures leads to crystalline and porous MgIm$_2$ [42]. At this point, it seemed opportune to extend the study by combining both alkali and alkaline earth metal centres, thus we recently reported the first bimetallic imidazolates containing alkali and alkaline earth metals, NaMgIm$_3$ and KMgIm$_3$ [40]. Both compounds are isostructural and crystallize in the hexagonal $P6_322$ space group. The crystal packing reveals channels with the empty volume calculated from the contact surface which is about 30 Å^3. Although the cage size recorder, ZIF-412 [43] with 38.1 Å, is able to selectively bind large volume volatile organic compounds, octane and p-xylene, AMgIm$_3$ with the cage diameter of 6.6 Å can still be applicable in gas sorption/separation processes. On the other hand, the preparation of manganese imidazolates remains a real challenge, probably due to the difficulties in forming an undistorted tetrahedral Mn^{2+} − 4 N geometry which is preferred in ZIFs. According to the Cambridge Crystallographic Data Centre database, only a few compounds with an undistorted tetrahedral Mn^{2+} − 4 N geometry are known [44–47]. It has been discussed in the literature that [Mn(Im)$_2$·2(ImH)] (ImH = imidazole) with distorted tetrahedral Mn^{2+} − 4 N (N − Mn − N is 99.86 − 126.45°) was synthesized from Mn$_2$(CO)$_{10}$ and melting ImH but this reaction produces CO and H$_2$ gases as by-products along with formation of the kinetically favoured framework [48]. Therefore, the formation of crystalline manganese imidazolate frameworks still remains an unsatisfied task and requires detailed research.

In this work, we report two new crystal structures of bimetallic imidazolates, AMnIm$_3$ (A = Na, K) which were solved using powder X-ray diffraction data measured at a synchrotron facility. The original intent of this work was to explore the possibility of forming coordination frameworks containing both the imidazolate and complex hydride anions as ligands. Although such a metal-hydride organic framework was not obtained, temperature-assisted

structural and microstructural analysis allowed a deeper understanding of the crystallization processes and reaction mechanisms occurring in the borohydride-imidazolate system. Extensive study of the thermal expansion behaviour revealed that the expansion of the bimetallic imidazolates does not proceed uniformly over the entire temperature range but rather abruptly changes from a colossal negative to a moderate positive volume expansion. Such behaviour is caused by the coherent intergrowth of the coexisting phases which form a composite, a positive lattice mismatch and a tensile strain during the coexistence of $NaMIm_3$ (M = Mg and Mn) and NaIm or HT-NaIm.

Experimental section

Synthesis

Four neat grinding mechanochemical reactions of $Mg(BH_4)_2$ or $Mn(BH_4)_2$ and AIm (A = Na, K) were conducted using a Planetary Micro Mill Fritsch Pulverisette 7 premium line. Reactants, together with stainless steel balls (d = 5 mm), were loaded into a stainless steel vial (25 ml) under inert conditions. Balls-to-sample mass ratio amounted to 25:1 in each reaction. Ball milling was performed at 550 rpm (10 min of milling, followed by a 5 min rest time; repeated 12 times). Molar ratios of reactants are given in Table 1. Anhydrous magnesium borohydride, $Mg(BH_4)_2$ (99.99%) as well as anhydrous manganese borohydride, $Mn(BH_4)_2$ were purchased from Sigma-Aldrich, while imidazolates AIm (A = Na, K) were prepared by the procedure reported elsewhere [39]. All handling and manipulation of the chemicals were performed in an argon-filled glovebox. All solvents have been dried on a vacuum line prior to the mechanochemical reactions.

Table 1 Reactants used for the mechanochemical synthesis

	Molar ratio of reactants
S1	$Mg(BH_4)_2$ and NaIm = 1:6
S2	$Mg(BH_4)_2$ and NaIm = 1:2
S3	$Mn(BH_4)_2$ and NaIm = 1:6
S4	$Mn(BH_4)_2$ and KIm = 1:6

X-ray powder diffraction (XRPD) at RT

XRPD measurements at room temperature (RT) were performed using a Stoe IPDS-P diffractometer with monochromated CuKα1 radiation (λ = 1.5406 Å) and a curved image plate detector, in Debye–Scherrer geometry. Air-sensitive samples were mounted in a glovebox in 0.8 borosilicate capillaries sealed with vacuum grease. Data were collected at RT, in 2θ range: $2 - 100°$ with counting time of 40 s/step. XRPD patterns are shown in Fig. S1 in the supporting information.

Synchrotron radiation X-ray powder diffraction (SR-XRPD) at HT

Synchrotron radiation experiments were done at the beamline BM01, SNBL at the ESRF, Grenoble, France. High temperature *in-situ* powder diffraction (HT-XRPD) data were collected with measurement parameters: $\lambda_{S1,S2}$ = 0.8187 Å, $\lambda_{S3,S4}$ = 0.7225 Å, sample rotation $0 - 40°$ and X-ray exposure time of 40 s. The air sensitive samples were mounted in 0.5 mm borosilicate capillaries and closed with vacuum grease. The Dectris Pilatus 2 M detector was used for recording 2D powder data at the sample to detector distances of 400 (samples S1 and S2) or 300 (samples S3 and S4) mm. The local program Bubble was used for integration of the 2D images [49]. Samples were heated by a heat blower from RT to 350 °C (with a 5 °C/min heating rate).

Structure solution and microstructural analysis

SR-PXD data were used for structure determination of new compounds. Indexing, space group determination and structure solution was carried out using Fox program [50]. Fullprof program [51] was used for Rietveld refinement [52] of the structural model. The visualizations of the crystal structures were made by programs VESTA [53] and Mercury [54]. Diffraction profiles of thermally treated samples were analysed by Rietveld refinement implemented in whole-powder-pattern modelling (WPPM) program MSTRUCT that is capable to determine the microstructure parameters such as micro-strain or crystallite size [55]. Software PASCal is used for calculation and visualization of thermal expansion behaviour [56].

Results and discussion

Thermal evolution of crystallization processes in borohydride-imidazolate system

The bimetalic imidazolate, NaMgIm$_3$, reported in our previous article [40], was prepared starting from Mg(BH$_4$)$_2$:NaIm in a 1:6 ratio. To gain a deeper understanding of the crystallization processes in the borohydride-imidazolate system an additional mechanochemical experiment was carried out using a different ratio of reactants, namely, Mg(BH$_4$)$_2$:NaIm in the 1:2 ratio. The 1:2 ratio (with less imidazolate than required for the formation of NaMgIm$_3$) was chosen to explore the possibility of forming bimetallic imidazolates that have a different stoichiometry than that reported. Interestingly, as the discussion will show, mechanochemical reaction performed in 1:2 ratio also resulted in the formation of NaMgIm$_3$. Nevertheless, as shown in Fig. 1, the temperature-induced structural evolution of the phases in samples S1 and S2 which occurs before and during the crystallization of NaMgIm$_3$, depends significantly on the initial amounts of imidazolate and borohydride.

At room temperature (RT), both mechanochemical reactions, performed in a 1:6 (S1) and 1:2 (S2) ratio, induce an ion exchange reaction leading to formation of NaBH$_4$. In both cases, the magnesium imidazolate, as the second product of the exchange reaction, becomes amorphous. In the case of the 1:6 reaction, where NaIm was used in excess, a certain amount of NaIm remained unreacted. Upon thermal treatment, the main difference is observed in terms of crystallization temperature of the bimetallic imidazolate; for an initial ratio of 1:2, the crystallization of NaMgIm$_3$ shifts to a higher temperature (from $\sim$ 120 °C, in the case of 1:6, to $\sim$ 220 °C for the 1:2 ratio). Such a pronounced difference in crystallization temperature is, in fact, a consequence of the different pathways, content-wise, that precede the crystallization of NaMgIm$_3$.

The mechanochemical reaction at RT can be described by Eq. 1:

$$Mg(BH_4)_2 + 2NaIm \rightarrow 2NaBH_4 + MgIm_{2(amorphous)} \tag{1}$$

The subsequent thermal treatment proceeds by different reaction routes depending on the NaIm excess: at high NaIm excess (sample S1), the bimetallic imidazolate NaMgIm$_3$ is formed at T = 125 °C by the reaction of the metal imidazolates (Eq. 2):

$$NaIm + MgIm_{2(amorphous)} \rightarrow NaMgIm_3 \tag{2}$$
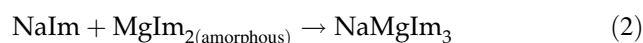
Upon further increase in temperature, NaIm undergoes the phase transition (at T = 209 °C) to its high-temperature polymorph. HT-NaIm melts above 224 °C (which is consistent with [41]), while NaBH$_4$ melts above 255 °C. Above 255 °C up to 346 °C the only crystalline phase in the sample is NaMgIm$_3$. This sample was heated up to 400 °C where NaMgIm$_3$ melts or decomposes (see sample S2 below) and cooled to RT, but NaMgIm$_3$ does not recrystallize.

On the other hand, in the sample S2 with starting ratio of 1:2, the mechanochemical reaction follows Eq. 1, but unlike sample S1, the temperature-induced crystallization of NaMgIm$_3$, follows the reaction between sodium borohydride and magnesium imidazolate as shown by Eq. 3:

$$2NaBH_4 + 3MgIm_{2(amorph.)} \rightarrow 2NaMgIm_3 + Mg(BH_4)_{2(amorph.)} \tag{3}$$
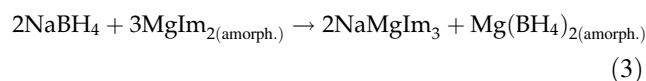
MgIm$_2$ crystallizes at T = 220 °C. Above 370 °C, the crystalline NaMgIm$_3$ melts or decomposes. Sample S2 was heated up to 450 °C and at this temperature MgIm$_2$ and NaBH$_4$ are present as crystalline phases in the system. It is interesting to note that the melting point of pure NaBH$_4$ is about 400 °C, so the higher melting point may be caused by the formation of an amorphous peritectic phase NaMg(BH$_4$)Im$_2$.

Our research was further extended to reactions between 3d transition metal borohydride Mn(BH$_4$)$_2$ and alkali metal (A = Na, K) imidazolates. The temperature-induced structural evolution of sample S3 (A = Na) is shown in Fig. 2.

Comparing the temperature-induced structural evolution of magnesium (S1) and manganese (S3) systems, both with the same initial ratio of borohydride to imidazolate of 1:6, reveals similar behaviour, although some important additional observations can be made. In the case of manganese, a mechanochemical reaction of Mn(BH$_4$)$_2$ and NaIm again resulted in a cation exchange leading to the formation of crystalline NaBH$_4$ and amorphous MnIm$_2$ (Eq. 4) but unlike in the case of magnesium, the excess of NaIm becomes amorphous.
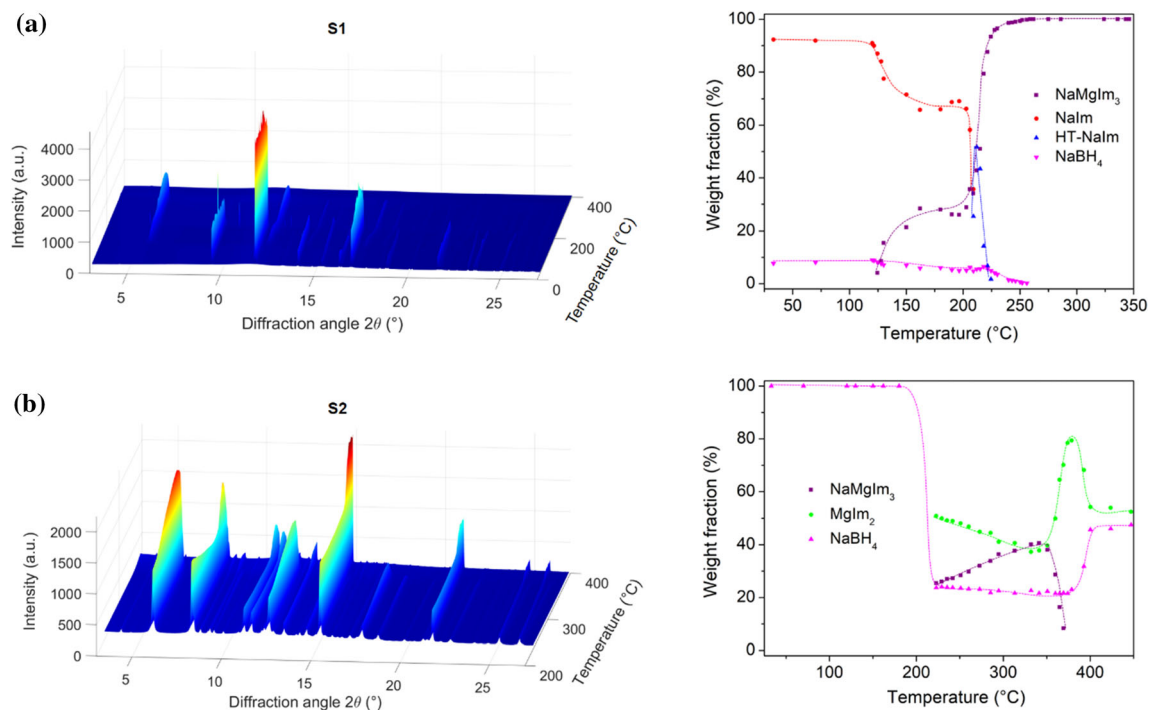
(a)

(b)

Figure 1 *In-situ* variable temperature XRPD data and changes in composition as a function of temperature for sample: **a** S1 and **b** S2. The orientation of the plot is chosen in such a way that no important data are hidden. Dashed lines represent guidelines for eye only.
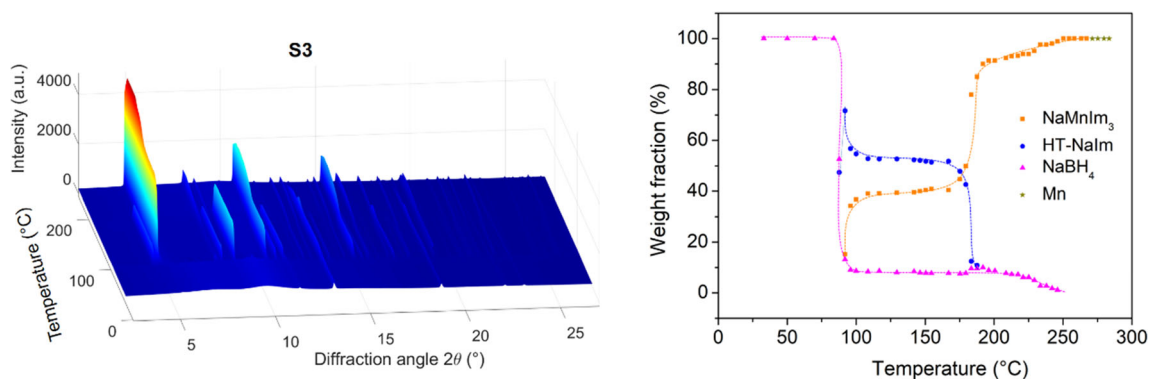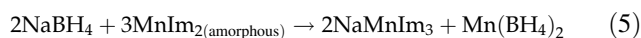

Figure 2 *In-situ* variable temperature XRPD data and changes in composition as a function of temperature for sample S3. The orientation of the plot is chosen in such a way that no important data are hidden. Dashed lines represent guidelines for eye only.

$$Mn(BH_4)_2 + 2NaIm \rightarrow 2NaBH_4 + MnIm_{2(amorphous)} \quad (4)$$

Although the milling conditions were identical to those of S1, it is plausible that the greater hardness of $Mn(BH)_4$, compared to $Mg(BH)_4$, causes the amorphization of NaIm. As the discussion will show, the observed mechanochemical amorphization of excess NaIm has important implications for the thermodynamic aspects of the phase transition to the high-temperature polymorph. Further thermal treatment (at $T \sim 90\ °C$) led to the crystallization of a new

phase, later recognized as $NaMnIm_3$, according to the reaction (Eq. 5):

$$2NaBH_4 + 3MnIm_{2(amorphous)} \rightarrow 2NaMnIm_3 + Mn(BH_4)_2 \quad (5)$$

Unlike in the case of the magnesium system (Eq. 2), here we observe the presence of the excess NaIm in its crystalline high-temperature form at the temperature of formation of the bimetallic imidazolate. It is particularly interesting to note that crystalline room-temperature NaIm, as present in the case of magnesium system, transforms to HT- crystalline
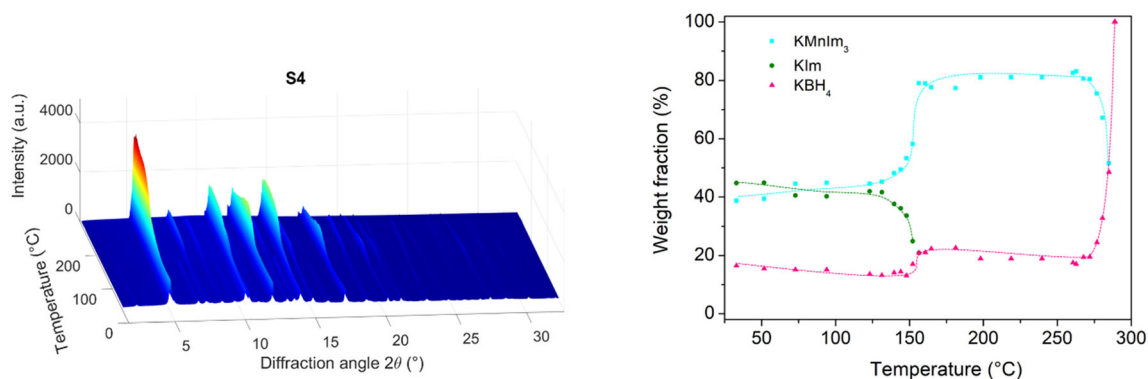
Figure 3 *In-situ* variable temperature XRPD data and changes in composition as a function of temperature for sample S4. The orientation of the plot is chosen in such a way that no important data are hidden. Dashed lines represent guidelines for eye only.

polymorph at T = 209 °C, whereas amorphous NaIm, as present in the manganese system, transforms to HT-polymorph at as low as 87 °C. With further increase in temperature, HT-NaIm remains crystalline up to 188 °C, while NaBH$_4$ remains crystalline up to 246 °C. At higher temperatures, only NaMnIm$_3$ is present in the sample and remains stable up to 280 °C. Above 272 °C, NaMnIm$_3$ decomposes and a small amount of metallic Mn crystallizes.

Finally, the mechanochemical reaction of Mn(BH$_4$)$_2$ and KIm (in a 1:6 ratio) was investigated (sample S4, Fig. 3).

While one would have expected similar products to the reaction between Mn(BH$_4$)$_2$ and NaIm, structural analysis showed that the new bimetallic KMnIm$_3$ had already crystallized, during ball-milling, according to the reaction which is equivalent to the sum of reactions (1) and (2):

$$Mn(BH_4)_2 + 3KIm \rightarrow 2KBH_4 + KMnIm_3 \qquad (6)$$

With further temperature increase, the excess KIm decomposes or melts at 155 °C, while KMnIm$_3$ remains stable from RT up to 285 °C. Above this temperature, it melts or decomposes and only KBH$_4$ remains crystalline in the sample. Equation 1–6 are overall equations for the mechanochemical reactions, while the partial equations encompassing all components present in the samples (including those that do not react with other phases) can be found in the supporting information (Eqs. S1-S7).

The thermal stability of the bimetallic magnesium and manganese imidazolates prepared in a 1:6 ratio is summarized in Table 2. It is observed that potassium manganese imidazolate is swiftly formed during milling at RT, while the additional thermal treatment is required to induce crystallization of the sodium bimetallic imidazolates. Manganese bimetallic imidazolates melt in the temperature range ∼ 280–290 °C, while the magnesium compounds remain stable up to ∼ 340–350 °C. This finding was expected considering that the degree of ionic *versus* covalent character is greater for the Mg-N bond than in the case of manganese. Since no recrystallization was observed in our experiments upon cooling of any bimetallic imidazolates, we conclude that the compounds decompose before melting.

Crystal structures of AMnIm$_3$ (A = Na, K)

Two new crystal structures, AMnIm$_3$ (A = Na, K) were solved from synchrotron X-ray powder diffraction data at elevated temperatures. A single phase pattern collected at 200 °C was used for structure determination of NaMnIm$_3$, while the crystal structure of KMnIm$_3$ was determined from the multiphase pattern collected at 173 °C. The Rietveld refinement plots for NaMnIm$_3$ and KMnIm$_3$ are given in Fig. 4. Crystal data and summary of structure refinement data are listed in Table 3.

Both compounds crystallize in a hexagonal system (space group $P6_322$). The positions of a Na (or K) atom, a Mn atom, and an imidazolate group were varied in Fox using the appropriate antibump restraints in order to determine the structure. The imidazolate ring was treated as a rigid body, only its position and orientation in the unit cell were warried. Interestingly, the structure determination of alkali manganese imidazolates is quite different from the structure solution process which gave a correct structure in the case of alkali magnesium

Table 2 Thermal stability of $AMIm_3$ (A = Na, K; M = Mg, Mn)

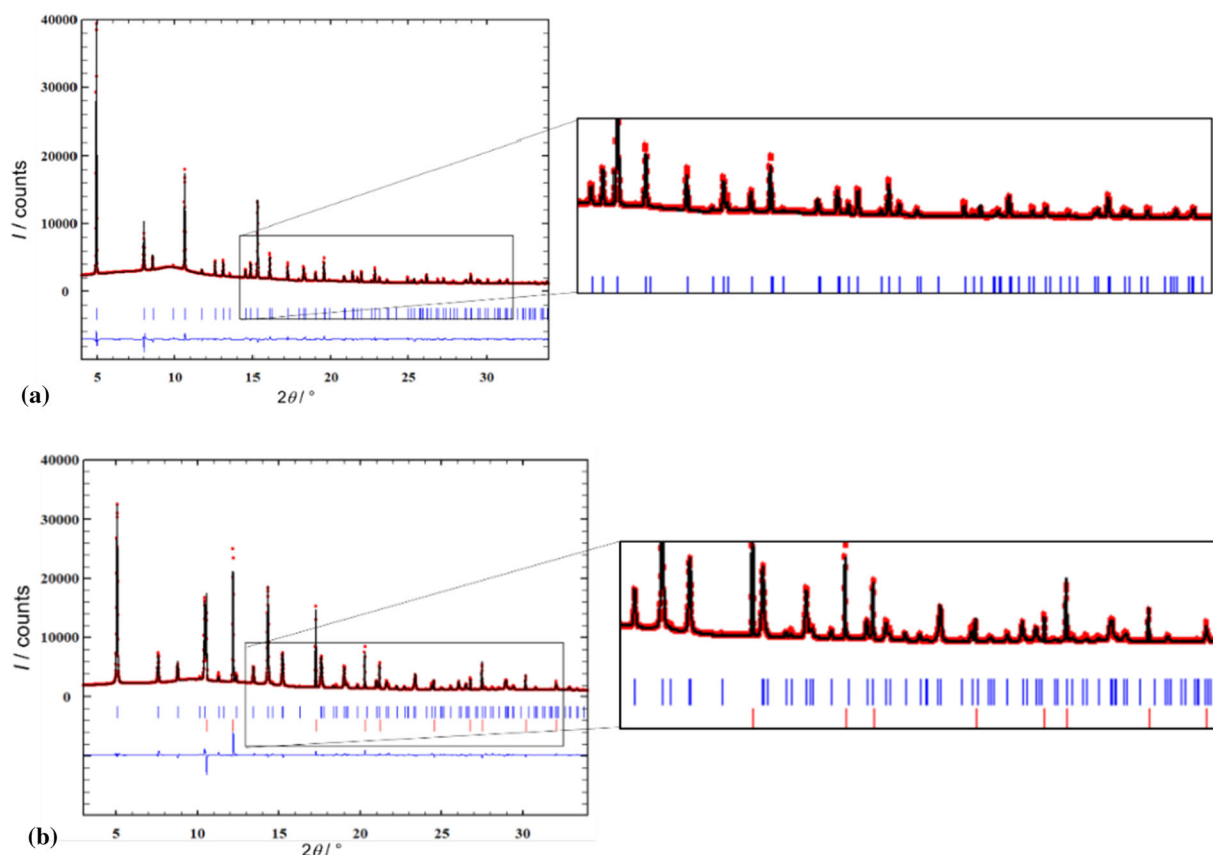| Compound	Stability range (°C)	Recrystallization
$NaMgIm_3$	Crystallization: 122 °C	No data
	Decomposition: 340 °C	
$NaMnIm_3$	Crystallization: 87 °C	No, only Mn is present during cooling back to RT
	Decomposition: 280 °C	
$KMnIm_3$	Crystallization: RT (during milling)	No, only KBH_4 is present during cooling back to RT
	Decomposition: 289 °C	

Figure 4 Rietveld refinement of **a** sample S3 used for the structural determination of $NaMnIm_3$. Vertical marks represent Bragg reflections of $NaMnIm_3$, and **b** sample S4 used for the structural determination of $KMnIm_3$. Blue vertical marks represent Bragg reflections of $KMnIm_3$ and red represents KBH_4. Experimental pattern is given as red dots, black curve shows calculated profile and the difference curve is given in blue. Enlarged part of diffraction pattern is shown to illustrate the quality of refinement.

imidazolates. For $AMgIm_3$ (A = Na, K), the parallel tempering procedure, with one billion trials per run, was a good choice, but this strategy, when applied to $AMnIm_3$ (A = Na, K) resulted in the false minimum structures, with doubled imidazolate rings. Therefore a different global optimization strategy was used for the structure solution of $AMnIm_3$ (A = Na, K). The correct structures were obtained by utilizing a small number of runs and trials with each run followed by a least squares refinement procedure [50]. One possible explanation is that the X-ray diffraction contrast between Na^+ and Mg^{2+} is practically zero, which makes the parameter space in the global optimization simpler, even if the false minima arise [57]. The false

Table 3 Crystal data and summary of structure refinement for NaMnIm$_3$ and KMnIm$_3$

	NaMnIm$_3$	KMnIm$_3$
Profile function	Pseudo voigt	Pseudo voigt
R (profile)/%	4.9	6.0
R (weighted profile)/ %	7.7	10.1
χ^2	$1.16 \cdot 10^3$	$5.16 \cdot 10^3$
Space group	$P6_322$	$P6_322$
a/Å	9.64595(13)	9.42292(15)
c/Å	6.57337(9)	7.33233(18)
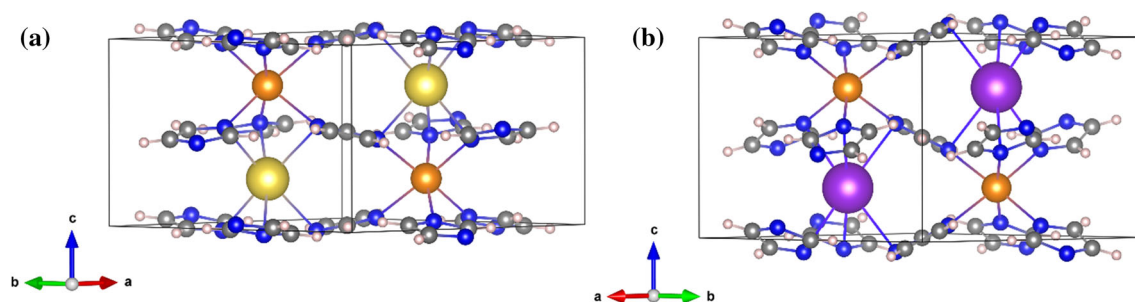
Figure 5 Crystal structure of **a** NaMnIm$_3$ and **b** KMnIm$_3$. Manganese atoms are shown as orange balls, sodium as yellow, potassium is given in purple, carbon is grey while nitrogen is shown in blue colour.

minima were eliminated and both the NaMnIm$_3$ and KMnIm$_3$ structures were validated by BVS calculations [58]. The crystal structures of NaMnIm$_3$ and KMnIm$_3$ are shown in Fig. 5.

In contrast to monometallic NaIm, in which the sodium exhibits tetrahedral coordination [39], in the structure of bimetallic AMnIm$_3$ (A = Na, K) both the alkali metal cation and the Mn cations exhibit distorted octahedral coordination. Each imidazolate is surrounded by four metal centres; two alkali metal and two manganese atoms. Although the crystal structures of NaMnIm$_3$ and KMnIm$_3$ are quite similar a difference is observed with respect to the polyhedra around the alkali atoms; in the case of NaMnIm$_3$ the octahedra around the sodium are more distorted than those around the potassium atoms in the case of KMnIm$_3$. Along the c-direction, the chains consisting of alternating A (A = Na, K) and Mn face-shared octahedra are formed from three imidazole rings via bridging nitrogen atoms. The chains running parallel to c-axis are additionally mutually connected by bridging imidazolate anions, forming zig-zag networks in the ab and ac planes, that eventually leads to a three-dimensional network (Fig. 6). It also reveals

the presence of channels running along the c-direction, and located on the 6_3 screw axis.

The empty volume of pores calculated by Mercury (Cambridge Crystallographic Data Centre) [54], located in the channels running parallel to c-axis, in AMIm$_3$ (A = Na, K, M = Mg, Mn) are given in Table 4.

Contact surface amounts to 35.2 Å^3 for NaMnIm$_3$ (assuming a spherical probe of r = 1.4 Å) and 30.8 Å^3 for KMnIm$_3$ (assuming a spherical probe of r = 1.2 Å). For comparison, Mn(BH$_4$)$_2$ has isolated voids with an estimated volume of 21 Å^3 [59–61]. It can be seen from Table 4 that NaMnIm$_3$ has the largest pore volume among the group AMIm$_3$ (A = Na, K; M = Mg, Mn), that amount to 6.6% of the unit cell volume, whereas KMgIm$_3$ contains pores covering only 4.1% of unit cell volume. This finding might be related to the more isotropic nature of interactions involving 3s orbitals of magnesium compared to directional interactions of 3d orbitals in the case of manganese, as well as to the fact that the imidazolate ring is almost parallel to the ab plane in the case of the sodium compound, while the potassium compound shows a pronounced ring tilting, leaving less free
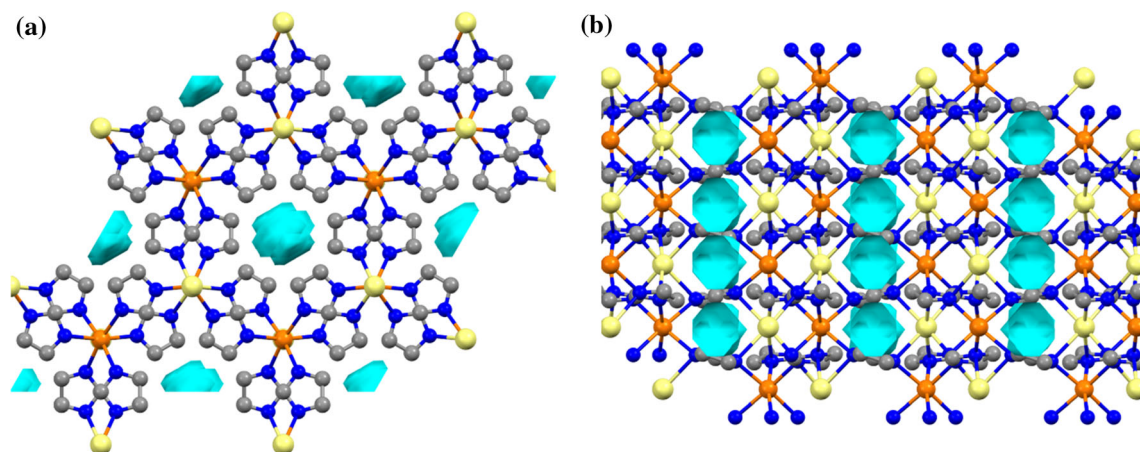
(a)

(b)

Figure 6 Crystal packing of NaMnIm$_3$ in ab and bc plane. Manganese atoms are shown as orange balls, sodium as yellow, potassium is given in purple, carbon is grey while nitrogen is shown in dark blue colour. Free volume in pores is represented as light blue spheres. Hydrogens are omitted for clarity.

Table 4 Bond length distances A $-$ N$_{im}$ and M $-$ N$_{im}$ and volume of pores in AMIm$_3$ (A = Na, K, M = Mg, Mn)

Compound	Bond length distances M-N$_{im}$	Empty volume in the pores	
NaMgIm$_3$	$d(Na_{oct} - N_{Im}) = 2.5851(2)$ Å	30.51 Å^3 (5.9% of unit cell volume)	This work
	$d(Mg_{oct} - N_{Im}) = 2.3701(2)$ Å	$r = 1.3$ Å	
KMgIm$_3$	$d(K_{oct} - N_{Im}) = 3.081(3)$Å	22.62 Å^3 (4.1% of unit cell volume)	Ref [40]
	$d(Mg_{oct} - N_{Im}) = 2.329(3)$ Å	$r = 1.1$ Å	
NaMnIm$_3$	$d(Na_{oct} - N_{Im}) = 2.6685(1)$ Å	35.19 Å^3 (6.6% of unit cell volume)	This work
	$d(Mn - N_{Im}) = 2.3722(1)$ Å	$r = 1.4$ Å	
KMnIm$_3$	$d(K_{oct} - N_{Im}) = 3.031(7)$Å	30.82 Å^3 (5.5% of unit cell volume)	This work
	$d(Mn_{oct} - N_{Im}) = 2.379(7)$ Å	$r = 1.2$ Å	

space. AMnIm$_3$ compounds are isostructural with their magnesium analogues reported in our previous paper, AMgIm$_3$ (A = Na, K) [40]. That was, in fact, quite expected if one considers the structural similarities between Mn- and Mg-borohydride compounds. The bond between the manganese atom and the nitrogen atom from the imidazolate ring in NaMnIm$_3$ [$d(Mn - N_{Im}) = 2.3722(1)$ Å] is slightly longer than the corresponding bond in NaMgIm$_3$ [$d(Mg - N_{Im}) = 2.3701(1)$ Å]. As it is also the case with borohydrides, larger Mn^{2+} in γ-Mn(BH$_4$)$_2$ forms a larger unit cell compared to γ-Mg(BH$_4$)$_2$ ($V_{NaMnIm3} = 529.674(18)$ Å^3, $V_{NaMgIm3} = 514.55(5)$ Å^3). The bond distance $d(Mn - N_{Im})$ which is 2.3722(1) Å also indicates the high spin state of manganese in NaMnIm$_3$ [62].

Thermal expansion behaviour

Rietveld refinement of the *in-situ* high temperature XRPD data revealed a complex nature of the crystallization pathways of the bimetallic imidazolates but also interesting trends in unit-cell expansion as a function of temperature. Table 5 gives the thermal expansion coefficients α along the a, b and c- directions for bimetallic imidazolates AMIm$_3$ (A = Na, K; M = Mg, Mn), as well as for monometallic imidazolates and borohydrides that are also present in different temperature intervals in samples S1-S4. The expansion coefficients were calculated in the temperature range given in Table 5. The temperature ranges do not necessarily represent the entire range in which a particular phase is present. Intervals near crystallization/transformation/decomposition/melting temperature were omitted due to uncertainty in

Table 5 Thermal expansion coefficients α along the *a*, *b* and *c*- direction for bimetallic imidazolates AMIm₃ (A = Na, K; M = Mg, Mn), metal imidazolates AImₓ (A = Na, K, Mg) and metal borohydrides ABH₄ (A = Na, K) in samples S1-S4

| α_i (×10⁻⁶K⁻¹)								
S1			**S2**	**S3**		**S4**		
NaMgIm₃			NaMgIm₃	NaMnIm₃		KMnIm₃		
150–209 °C	212–224.5 °C	227–343.2 °C	222.8–359 °C	92–187.7 °C	191–279.8 °C	33–94 °C	156.4–284.9 °C	
a −181(8)	−82(7)	−9(2)	−19(1)	−113(1)	−14(2)	−16(1)	−15(1)	
c −210(8)	−57(5)	34(5)	41(1)	−56(0)	52(3)	83(7)	117(3)	
NaIm	HT-NaIm		MgIm₂	HT-NaIm		KIm		
33–209 °C	209–215 °C		222.8–423 °C	108–187.7 °C		33–152.2 °C		
a 80(3)	113(19)		33(1)	7(1)		84(2)		
b −27(1)								
c 104(5)	197(0)		−11(0)	148(7)		31(2)		
NaBH₄			NaBH₄	NaBH₄		KBH₄		
33–256 °C			33–447 °C	33–212 °C		T = 33–289 °C		
a 71(1)			72(1)	76(2)		86(0)		
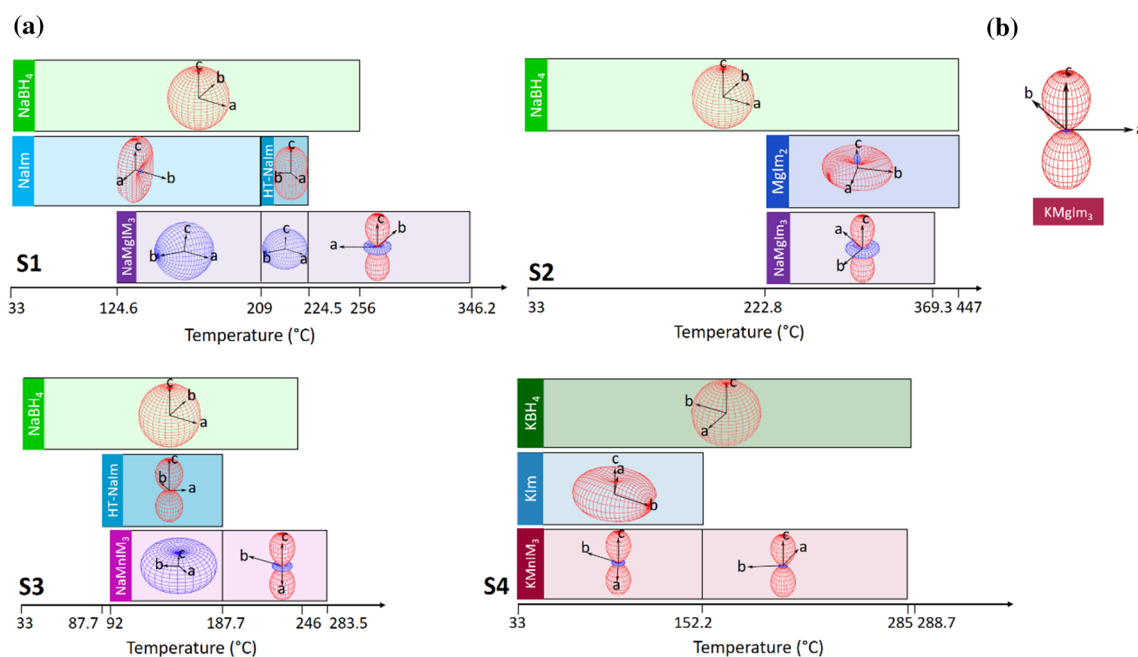
Figure 7 Thermal indicatrices of phases present in samples **a** S1-S4, **b** KMgIm₃.

determining unit-cell parameters when the amount of phase is small.

Thermal indicatrices for each crystalline phase in samples S1-S4 are shown in Fig. 7. Thermal expansion often exhibits similar trends typical of each type of structure. It can be seen that sodium- and potassium- borohydrides (present in samples S1-S3 and S4, respectively) exhibit large positive isotropic linear thermal expansions with large volumetric expansion in the range $217(2) \times 10^{-6}$ K⁻¹ $< \alpha_V < 265(2) \times 10^{-6}$ K⁻¹, which is comparable to the thermal expansion values reported for other metal borohydrides ($\alpha_{V-} = 260 - 290 \times 10^{-6}$ K⁻¹ for LiBH₄) [63].

In addition, magnesium and sodium imidazolates (contained in samples S1 and S2, respectively) exhibit similar thermal behaviour. Both exhibit large positive

expansion along two directions accompanied by a uniaxial negative thermal expansion in the third direction. A similar shape of thermal indicatrix is found in the case of the potassium imidazolate present in sample S4; large positive expansions along two directions are this time, accompanied by a small positive expansion along the third axis. On the other hand, the high-temperature polymorph of NaIm shows a different behaviour from the room-temperature phase; the HT phase exhibits a small expansion along two directions coupled with a large expansion along the third direction. All compounds show a positive overall volume expansion despite a uniaxial negative expansion in the case of $MgIm_2$ and NaIm; of all, KIm exhibits the largest volume expansion $\alpha_V = 196(9) \times 10^{-6} \ K^{-1}$.

A particularly interesting thermal behaviour was observed for $AMIm_3$ (A = Na, K; M = Mg, Mn), present in samples S1-S4; Fig. 7 shows that in some cases the expansion of bimetallic imidazolates is not uniform over the entire temperature range yet it abruptly changes from colossal negative values of overall volume expansion to moderate positive overall volume expansion. Since the turning point of $NaMgIm_3$ (in sample S1) at $T \sim 224$ °C also represents the temperature at which the crystalline HT-NaIm is no longer present in the sample, it is clear that the thermal behaviour of the bimetallic imidazolate is significantly affected by the additional crystalline phases in each sample. Before elaborating the reasons for such a behaviour, it is worth discussing the thermal behaviour of isostructural $KMgIm_3$ reported in our previous work [40]. The thermal behaviour of $KMgIm_3$, present in the sample without any other crystalline phases, is shown in Fig. 7b. Indeed, comparing the indicatrix of $KMgIm_3$ with the indicatrices of $NaMgIm_3$, $NaMnIm_3$ and $KMnIm_3$ in samples S1-S4, it is clear that all bimetallic imidazolates $AMIm_3$ (A = Na, K; M = Mg, Mn) show large positive expansion along the c-direction coupled with small biaxial negative expansions, over a certain temperature range (above ~ 220 °C for $NaMgIm_3$, above ~ 180 °C for $NaMnIm_3$ while $KMnIm_3$ exhibits such a behaviour over the entire temperature range).

Let us now return to the temperature range where $NaMIm_3$ (M = Mg, Mn) experiences a large negative expansion in all three directions. Given the phase composition of samples S1 and S3, a plausible explanation for such a behaviour seems to be related

to the composite formation and coherent intergrowth of $NaMIm_3$ with either NaIm, HT-NaIm or $NaBH_4$. However, it is be noted that both $NaMgIm_3$ and $NaMnIm_3$ abruptly change their expansion trend once crystalline NaIm and/or HT-NaIm are no longer present in the sample suggesting that the intergrowth of bimetallic imidazolate and alkali imidazolate may be responsible for the observed change of thermal expansion behaviour. The intergrowth of $NaMgIm_3$ and NaIm in the temperature range $T = 124.6 - 209$ °C was studied in detail; by carefully examining the structures present in sample S1, an epitaxial relationship between the 100 plane of hexagonal $NaMgIm_3$ and the 001 plane of orthorhombic NaIm was found and shown in Fig. 8.

It can be seen that the b-parameters of $NaMgIm_3$ and NaIm are similar. Also, the c parameter of $NaMgIm_3$ is closely related to the a parameter of NaIm. Figure 8b shows the 100–001 interface enabling coherent intergrowth of two phases. In general, an interface can be coherent, semi-coherent or incoherent, depending upon the lattice misfit at the interface. If the adjacent layers are assumed to consist of two crystalline phases, 1 and 2, and that both materials are elastically deformable, then there is lattice mismatch due to the difference in lattice constants but the interfaces are still coherent:

$$f_{1/2} = \frac{d_{hkl,2} - d_{hkl,1}}{d_{hkl,1}} \quad \text{and} \quad f_{2/1} = \frac{d_{hkl,1} - d_{hkl,2}}{d_{hkl,2}}$$

where $f_{1/2}$ is the mismatch of phase 1 relative to phase 2 and $f_{2/1}$ the mismatch of 2 relative to 1. The mismatch between coherent phases is often small, typically less than $\pm 5\%$ [64, 65]. Calculated lattice mismatches at the interface between $NaMgIm_3$ and NaIm at different temperatures (130 °C $-$ 180 °C) are small, ranging from 1.6 to $\pm 4.8\%$, therefore enabling the formation of coherent interface. At $T = 162$ °C, the lattice parameters of $NaMgIm_3$ amount to $b = 9.613$ Å and $c = 6.654$ Å and those of NaIm $b = 10.037$ Å, $a = 6.769$ Å. The lattice mismatch, as shown in Fig. 8c, amounts to $+ 4.4\%$ along the b-direction and $+ 1.7\%$ along the c-direction of $NaMgIm_3$ (i.e. b-direction of NaIm). Despite the observed lattice mismatch, Fig. 9 shows well-formed coherent intergrowths between the bc plane of $NaMgIm_3$ (purple) and the ab plane of NaIm (turquoise).

From the lattice mismatch, a tensile strain ε_0 was calculated according to the formula: $f_{1/2} \approx -f_{\bar{2}} \approx 2\varepsilon_{0,1} = -2\varepsilon_{0,2} = 2\varepsilon_0$. In the c-direction of
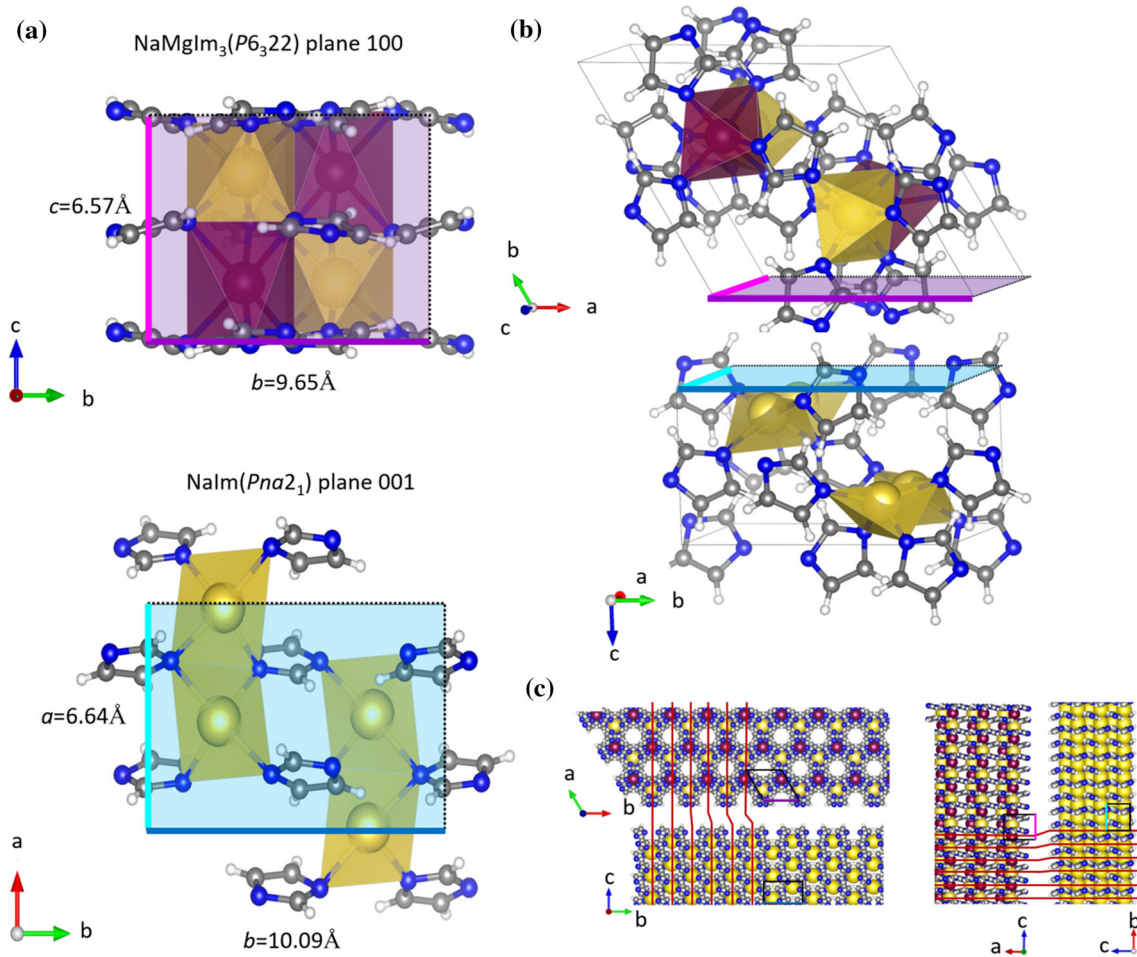
Figure 8 **a** Epitaxial relationship between planes 100 (NaMgIm₃) and 001 (NaIm), **b** Intergrowth interface of 100 NaMgIm₃ and 001 NaIm, **c** Lattice mismatch between NaMgIm₃ and NaIm.
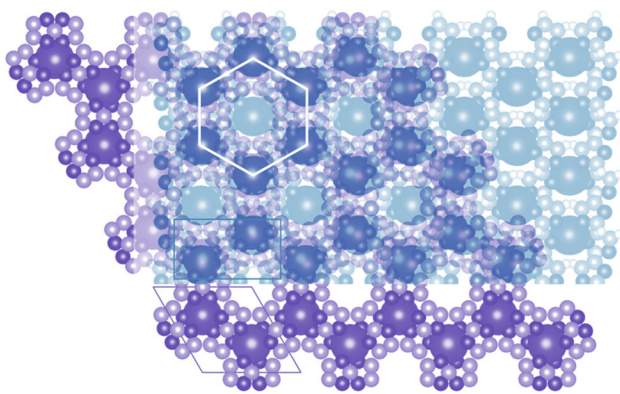

Figure 9 Overlapped coherently intergrown 100 plane of NaMgIm₃ and 001 plane of NaIm.

NaMgIm₃ (i.e. b-direction of NaIm), the tensile strains is $+\,0.85\%$, while the strain in the b-direction equals 2.2%. The elastic properties in both phases are assumed to be similar, so that the interface strain will be divided approximately in equal parts by both adjacent phases: $\varepsilon_{0,1} \approx -\varepsilon_{0,2}$ [64]. Upon further temperature increase, above 209 °C, NaIm transforms to its HT polymorph. Similar to NaIm, NaMgIm₃ forms an intergrowth relationship with the HT-polymorph of NaIm which continues to affect the thermal expansion behaviour in a similar manner. Above 224.6 °C, once the crystalline HT-NaIm is no longer present in the samples, NaMgIm₃ begins to exhibit thermal expansion behaviour that is intrinsic to the structure of bimetallic imidazolates. A similar effect of composite coherent intergrowth can be noticed in sample S3. In the temperature range $T = 92 - 187.7$ °C NaMnIm₃ exhibit negative thermal expansion along all three directions as a consequence of the intergrowth with HT-NaIm. Once the crystalline HT-NaIm is no longer present in the sample, NaMnIm₃ begins to show a large positive expansion
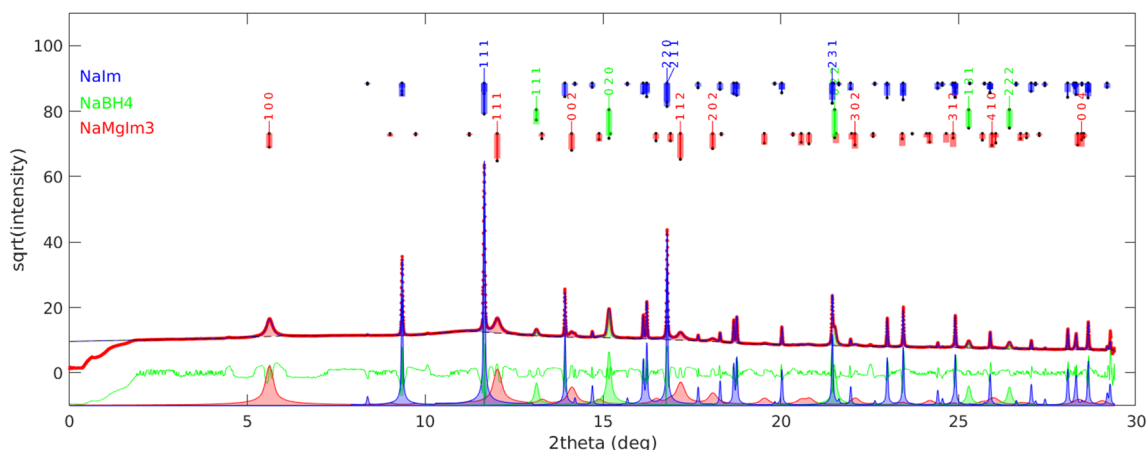
Figure 10 XRD pattern for S1 collected at temperature $T = 127$ °C and fitted by WPPM method in order to obtain microstructure parameters. The individual contributions from different phases on the final pattern are plotted on the baseline of the graph.

along the c-direction that is coupled with small biaxial negative expansions along the a and b-axis.

The results shown in Fig. 7, also show that NaMgIm$_3$ in sample S2 (coexisting with MgIm$_2$) exhibits the same trend of thermal expansion (throughout the temperature range from 222.8 to 369.3 °C) as in sample S1 once the crystalline sodium imidazolate is no longer present in the sample (above 224.5 °C). This means that MgIm$_2$ and NaMgIm$_3$ do not form any epitaxial-like relationship that could affect their thermal expansion. The same was found for KMnIm$_3$ in sample S4; KMnIm$_3$ exhibit similar expansion behaviour regardless of the presence/absence of the crystalline KIm in the sample. The reason for this is probably too great a difference in the crystal structures of AMIm$_3$ (A = Na, K; M = Mg, Mn) compounds and MgIm$_2$ or KIm, while sodium imidazolates have comparable structures to AMIm$_3$ (A = Na; M = Mg, Mn).

Finally, it is important to address the values of linear thermal expansion. As shown in Table 5, the sodium bimetallic imidazolates, when they do not experience any epitaxial relationship, show a small negative expansion along the a-axis, ranging from $\alpha_a = -9(2) \times 10^{-6}$ K^{-1} (in the case of NaMgIm$_3$) to $\alpha_a = -16(1) \times 10^{-6}$ K^{-1} (for KMnIm$_3$), which is accompanied by a moderate to large positive expansion along the c-axis, ranging from $\alpha_c = 34(5) \times 10^{-6}$ K^{-1} (for NaMgIm$_3$) to $\alpha_c = 117 \times 10^{-6}$ K^{-1} (for KMnIm$_3$). On the other hand, when bimetallic imidazolates coexist with phases that enable the coherent intergrowth, their thermal expansion coefficients abruptly shift to colossal negative values along all

axes for example $\alpha_a = -181(8) \times 10^{-6}$ K^{-1} and $\alpha_c = -210(8) \times 10^{-6}$ K^{-1} in the case of NaMgIm$_3$.

Microstructure

Heat treatment did not only affect lattice parameters but also microstuctural features of the crystalline phases. To correlate the microstructure parameters with the thermal expansion behaviour of NaMgIm$_3$ in S1, we performed a Rietveld/WPPM refinement with program MSTRUCT for collected *in-situ* XRD patterns of S1. The typical fitted pattern is shown in Fig. 10.

In the whole temperature range, the peak width of the NaIm phase corresponds to the instrumental broadening implying negligible microstrain (below 0.1%) and a large crystallite size above the detection limit (300 nm). The same is true for the high temperature polymorph of NaIm. The crystallites of NaBH$_4$ also did not exhibit detectable microstrain, however we observed a linear dependence of the crystallite size on temperature, explicitly ranging from 10 nm at room temperature to about 100 nm at 200 °C. Above 200 °C, the crystallite sizes abruptly increased beyond the detection limit.

On the other hand, the microstructure of NaMgIm$_3$ evolved quite specifically in all three temperature ranges with different thermal expansion behaviour, as shown in Fig. 11. In the first temperature range (up to 209 °C), where the thermal expansion has the highest negative values, the crystallite sizes grow rather slowly and linearly from 25 to $\sim$ 40 nm. At the same time, the microstrain, which occurs at the
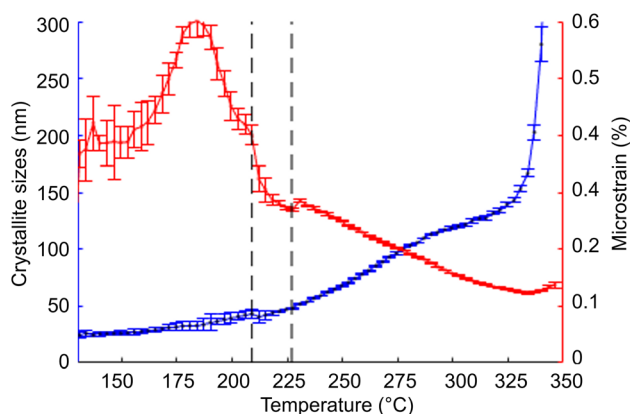
Figure 11 Temperature dependence of the crystallite size (blue) and the microstrain (red) for NaMgIm$_3$ phase in S1. Vertical dashed lines located at temperatures 209 °C and 227 °C indicate temperature regions with different thermal expansion behaviour.

very beginning of the phase formation, increases and reaches its maximum at 185 °C. If one recalls Fig. 1, this is the temperature at which NaMgIm$_3$ is fully formed and further consumption of NaIm is almost stopped. From this point on, the microstrain is slowly released back to initial value. Further change in trend occurs at the very temperature at which NaIm undergoes the phase transformation to its high-temperature phase. Suddenly, the microstrain in NaMgIm$_3$ decreases steeply, while the crystallite size growth rate of remains unaffected.

In the last temperature range, when NaIm melts, both the microstrain and the crystallite size of NaMgIm$_3$ followed more or less linear trend. As one would expect for annealing connected with crystal quality improvement, the microstrain was decreasing, while the crystallites were growing. Moreover, the slope of crystallite size growth rate was suddenly higher which could be an indication that the NaIm crystallites slowed down this process before they were melted.

Finally, it should be stressed out that the microstrain is defined as a relative width of the interplanar-distances distribution and this variance can originate from various reasons. However, such possible source in case of very small particle can be an inhomogeneous strain field being a result of interplay between elastically relaxed parts of surface and parts of surface coherently intergrown with mismatched lattice of other extraneous particle. The idea of intergrowth is strongly supported by the fact that the microstrain

evolution observed in the NaMgIm$_3$ clearly correlates with the following: firstly, the rate of the reaction where NaMgIm$_3$ is formed and NaIm is consumed, and secondly with the temperature of phase transformation of NaIm into its high temperature phase. Moreover, the microstrain is significantly released when the NaIm particles are being melted.

Conclusions

In the search for borohydride-imidazolate frameworks, we have discovered novel bimetallic imidazolates AMnIm$_3$ (A = Na, K). Thermal expansion of isostructural AMIm$_3$ (A = Na, K; M = Mg, Mn) compounds was studied in detail. An abrupt change in the thermal expansion of NaMIm$_3$ (M = Mg, Mn) was noticed when the composite with NaIm and/or HT-NaIm forms; the thermal volume expansion coefficient changes from moderately positive volume expansion for pure bimetallic imidazolate ($\alpha_a = -9(2) \times 10^{-6}$ K^{-1}, $\alpha_c = 34(5) \times 10^{-6}$ K^{-1}) to colossal negative values when composite is formed ($\alpha_a = -181(8) \times 10^{-6}$ K^{-1} and $\alpha_c = -210(8) \times 10^{-6}$ K^{-1}). Also, it is important to notice that composite material exhibit thermal expansion that is dramatically different from thermal expansion of both of its constituents. This work demonstrates that synthesis of materials containing coherent composites, together with variation of their volume fractions in the composite, can open the way for targeted design of zero thermal expansion materials.

Data availability

CCDC 2126064-2126065 contain the supplementary crystallographic data for this paper. These data can be obtained free of charge via www.ccdc.cam.ac.uk/data_request/cif, or by emailing data_request@ccdc.cam.ac.uk, or by contacting The Cambridge Crystallographic Data Centre, 12 Union Road, Cambridge CB2 1EZ, UK; fax: + 44 1223 336033.

Declarations

Conflict of interest The authors declare that they have no known competing financial interests or personal relationships that could have appeared to influence the work reported in this paper.

Supplementary Information: The online version contains supplementary material available at https://doi.org/10.1007/s10853-022-07360-z.

References

[1] Ren Z, Zhao R, Chen X, Li M, Li X, Tian H, Zhang Z, Han G (2018) Mesopores induced zero thermal expansion in single-crystal ferroelectrics. Nat Commun 9:1638. https://doi.org/10.1038/s41467-018-04113-y

[2] Miller W, Smith CW, Mackenzie DS, Evans KE (2009) Negative thermal expansion: a review. J Mater Sci 44:5441–5451. https://doi.org/10.1007/s10853-009-3692-4

[3] Mary TA, Evans JSO, Vogt T, Sleight AW (1996) Negative thermal expansion from 0.3 to 1050 Kelvin in ZrW_2O_8. Science 272:90–92. https://doi.org/10.1126/science.272.5258.90

[4] Phillips AE, Goodwin AL, Halder GJ, Southon PD, Kepert CJ (2008) Nanoporosity and exceptional negative thermal expansion in single-network cadmium cyanide. Angew Chem Int Ed 47:1396–1399. https://doi.org/10.1002/anie.200704421

[5] Attfield JP (2011) A fresh twist on shrinking materials. Nature 480:465–466. https://doi.org/10.1038/480465a

[6] Greve BK, Martin KL, Lee PL, Chupas PJ, Chapman KW, Wilkinson AP (2010) Pronounced negative thermal expansion from a simple structure: cubic ScF_3. J Am Chem Soc 132:15496–15498. https://doi.org/10.1021/ja106711v

[7] Takenaka K, Okamoto Y, Shinoda T, Katayama N, Sakai Y (2017) Colossal negative thermal expansion in reduced layered ruthenate. Nat Commun 8:14102. https://doi.org/10.1038/ncomms14102

[8] Liu Z, Gao Q, Chen J, Deng J, Lin K, Xing X (2018) Negative thermal expansion in molecular materials. ChemComm 54:5164–5176. https://doi.org/10.1039/C8CC01153B

[9] Dubbeldam D, Walton KS, Ellis DE, Snurr RQ (2007) Exceptional negative thermal expansion in isoreticular metal-organic frameworks. Angew Chem Int Ed 46:4496–4499. https://doi.org/10.1002/anie.200700218

[10] Goodwin AL, Calleja M, Conterio MJ, Dove MT, Evans JSO, Keen DA, Peters L, Tucker MG (2008) Colossal positive and negative thermal expansion in the framework material $Ag_3[Co(CN)_6]$. Science 319:794. https://doi.org/10.1126/science.1151442

[11] Panda MK, Centore R, Causà M, Tuzi A, Borbone F, Naumov P (2016) Strong and anomalus thermal expansion precedes the thermosalient effect in dynamic molecular crystals. Sci Rep 6:29610. https://doi.org/10.1038/srep29610

[12] Panda MK, Runčevski T, Sahoo SC, Belik AA, Nath NK, Dinnebier RE, Naumov P (2014) Colossal positive and negative thermal expansion and thermosalient effect in a pentamorphic organometallic martensite. Nat Commun 5:4811. https://doi.org/10.1038/ncomms5811

[13] Yamamoto H, Imai T, Sakai Y, Azuma M (2018) Colossal negative thermal expansion in electron-doped $PbVO_3$ Perovskites. Angew Chem Int Ed 57:8170–8173. https://doi.org/10.1002/anie.201804082

[14] Murray CB, Kagan CR, Bawendi MG (2000) Synthesis and characterization of monodisperse nanocrystals and close-packed nanocrystal assemblies. Annu Rev Mater Sci

30:545–610. https://doi.org/10.1146/annurev.matsci.30.1.545

[15] Alivisatos AP (1996) Semiconductor clusters, nanocrystals, and quantum dots. Science 271:933–937. https://doi.org/10.1126/science.271.5251.933

[16] Heath JR (1999) Nanoscale materials. Acc Chem Res 32:388–388

[17] Puntes VF, Krishnan KM, Alivisatos AP (2001) Colloidal nanocrystal shape and size control: the case of cobalt. Science 291:2115–2117. https://doi.org/10.1126/science.1057553

[18] Pan ZW, Dai ZR, Wang ZL (2001) Nanobelts of semiconducting oxides. Science 291:1947–1949. https://doi.org/10.1126/science.1058120

[19] Mittemeijer EJ, Scardi P (eds) (2013) Diffraction analysis of the microstructure of materials. Springer Science & Business Media. https://doi.org/10.1007/978-3-662-06723-9

[20] Hu J-X, Xu Y, Meng Y-S, Zhao L, Hayami S, Sato O, Liu T (2017) A material showing colossal positive and negative volumetric thermal expansion with hysteretic magnetic transition. Angew Chem Int Ed 56:13052–13055. https://doi.org/10.1002/anie.201707258

[21] Yuan X, Sun Y, Guo H, Shi K, Song P, Han H, Cui J, An S, Huang R, Li L, Wang C (2021) Design of negative/nearly zero thermal expansion behavior over a wide temperature range by multi-phase composite. Mater Des 203:109591. https://doi.org/10.1016/j.matdes.2021.109591

[22] Ding L, Wang Y, Na Chu L, Yan J (2011) Preparation and near zero thermal expansion property of $Mn_3Cu_{0.5}A_{0.5}N$ (A=Ni, Sn)/Cu composites. Scr Mater 65:687–690. https://doi.org/10.1016/j.scriptamat.2011.07.008

[23] Miao J, Liu J, Wu X, Zou H, Sha D, Ren J, Dai Y, Yan X, Cheng X (2018) Thermal expansion, electrical conductivity and hardness of $Mn_3Zn_{0.5}Sn_{0.5}N$/Al composites. Sci Eng Compos Mater 25:95–100. https://doi.org/10.1515/secm-2015-0402

[24] Takenaka K, Ichigo M (2014) Thermal expansion adjustable polymer matrix composites with giant negative thermal expansion filler. Compos Sci Technol 104:47–51. https://doi.org/10.1016/j.compscitech.2014.08.029

[25] Lin JC, Tong P, Zhang K, Ma XH, Tongm HY, Guo XG, Yang C, Wu Y, Wang M, Lin S, Song WH, Sun YP (2017) The GaNMn3-epoxy composites with tunable coefficient of thermal expansion and good dielectric performance. Compos Sci Technol 146:177–182. https://doi.org/10.1016/j.compscitech.2017.04.028

[26] Zhao W, Sun Y, Liu Y, Shi K, Lu H, Song P, Wang L, Han H, Yuan X, Wang C (2018) Negative thermal expansion over a wide temperature range in Fe-doped MnNiGe composites. Front Chem 6:15. https://doi.org/10.3389/fchem.2018.00015

[27] Yan XH, Miao JJ, Liu JQ, Wu X, Zou H, Sha DW, Ren J, Dai Y, Wang JJ, Cheng XN (2016) Zero thermal expansion, electrical conductivity and hardness of $Mn_3Zn_{0.5}Sn_{0.5}N$/Cu composites. J Alloy Compd 677:52–56. https://doi.org/10.1016/j.jallcom.2016.03.221

[28] Takenaka K, Hamada D, Kasugai D, Sugimoto N (2012) Tailoring thermal expansion in metal matrix composites blended by antiperovskite manganese nitrides exhibiting giant negative thermal expansion. J Appl Phys 112:9. https://doi.org/10.1063/1.4759121

[29] Takenaka K, Kuzuoka K, Sugimoto N (2015) Matrix-filler interfaces and physical properties of metal matrix composites with negative thermal expansion manganese nitride. J Appl Phys. https://doi.org/10.1063/1.4929363

[30] Zhou C, Zhang Q, Tan X, Deng S, Shi K, Wu G (2019) Fully-dense Mn3Zn$_{0.7}$Ge$_{0.3}$N/Al composites with zero thermal expansion behavior around room temperature. Materialia 6:100289. https://doi.org/10.1016/j.mtla.2019.100289

[31] Cen D, Wang B, Chu R, Gong Y, Xu G, Chen F, Xu F (2020) Design of (Hf, Ta)Fe$_2$/Fe composite with zero thermal expansion covering room temperature. Scr Mater 186:331–335. https://doi.org/10.1016/j.scriptamat.2020.05.048

[32] Guo XG, Tong P, Lin JC, Yang C, Zhang K, Wang M, Wu Y, Lin S, Song WH, Sun YP (2017) Large negative thermal expansion in $(Ga_{0.7}Cu_{0.3})_{1-x}Mn_xNMn_3$ (x ≤ 0.4), compensating for the thermal expansion of cryogenic materials. Scr Mater 128:74–77. https://doi.org/10.1016/j.scriptamat.2016.10.002

[33] Yan J, Sun Y, Wang C, Chu LH, Shi ZX, Deng SH, Shi KW, Lu HQ (2014) Study of structure of $Mn3Cu_{0.5}Ge_{0.5}N$/Cu composite with nearly zero thermal expansion behavior around room temperature. Scr Mater 84–85:19–22. https://doi.org/10.1016/j.scriptamat.2014.04.010

[34] Mohn P (1999) A century of zero expansion. Nature 400:18–19. https://doi.org/10.1038/21778

[35] Salvador JR, Guo F, Hogan T, Kanatzidis MG (2003) Zero thermal expansion in YbGaGe due to an electronic valence transition. Nature 425:702–705. https://doi.org/10.1038/nature02011

[36] Chen J, Fan L, Ren Y, Pan Z, Deng J, Yu R, Xing X (2013) Unusual transformation from strong negative to positive thermal expansion in $PbTiO_3$-$BiFeO_3$ perovskite. Phys Rev Lett 110:115901. https://doi.org/10.1103/PhysRevLett.110.115901

[37] Zhou H-C, Long JR, Yaghi OM (2012) Introduction to metal-organic frameworks. Chem Rev 112:673–674. https://doi.org/10.1021/cr300014x

[38] Yaghi OM, Kalmutzki MJ, Diercks CS (2019) Introduction to reticular chemistry: metal-organic frameworks and

covalent organic frameworks, first edition. Wiley-VCH Verlag GmbH & Co. KGaA, https://doi.org/10.1002/anie.201906230

[39] Morelle F (2017) Hybrid hydridic frameworks by the combination of complex hydrides and nitrogen-based organic ligands. Ph.D. Dissertation, Univerité catholique de Louvain, Louvain-la-Neuve, Belgium

[40] Burazer S, Morelle F, Filinchuk Y, Černý R, Popović J (2019) Mixed-metal imidazolates containing alkali and alkaline earth metals: Mechanochemical synthesis and crystal structure of AMgIm$_3$ (A = Na or K). Inorg Chem 58:6927–6933. https://doi.org/10.1021/acs.inorgchem.9b00446

[41] Burazer S, Robeyns K, Guénée Mali G, Morelle F, Ban V, KlaserT FY, Černý R, Popović J (2021) Quenchable porous high-temperature polymorph of sodium imidazolate. NaIm Cryst Growth Des 21:770–778. https://doi.org/10.1021/acs.cgd.0c01006

[42] Safin DA, Robeyns K, Filinchuk Y (2016) Magnesium imidazolate - a first porous zeolitic imidazolate framework with alkali and alkaline earth metals. Acta Crystallogr, Sect A: Found Adv 72(1):402. https://doi.org/10.1107/S2053273316094134

[43] Yang J, Zhang Y-B, Liu Q, Trickett CA, Gutiérrez-Puebla E, Monge MA, Cong H, Aldossary A, Deng H, Yaghi OM (2017) Principles of designing extra-large pore openings and cages in zeolitic imidazolate frameworks. J Am Chem Soc 139, 6448−6455, https://doi.org/10.1021/jacs.7b02272

[44] Lewis RA, Wu G, Hayton TW (2011) Stabilizing high-valent metal ions with a ketimide ligand set: synthesis of n(N-CtBu$_2$)$_4$. Inorg Chem 50:4660–4668. https://doi.org/10.1021/ic200490v

[45] Putzer MA, Pilz A, Müller U, Neumüller B, Amido-Komplexe von Mangan(II) DK (1998) Synthese und Kristallstrukturen von [Mn(NPh$_2$)$_2$(THF)]$_2$ und Na$_2$[Mn(NPh$_2$)$_4$]·2 C$_7$H$_8$. Z. Anorg Allg Chem 624, 1336−1340, https://doi.org/10.1002/(SICI)1521-3749(199808)624:8<1336::AID-ZAAC1336>3.0.CO;2-3

[46] Karadas F, Avendano C, Hilfiger MG, Prosvirin AV, Dunbar KR (2010) Use of a rhenium cyanide nanomagnet as a building block for new clusters and extended networks. Dalton Trans 39:4968–4977. https://doi.org/10.1039/B927242A

[47] Milon J, Daniel MC, Kaiba A, Guionneau P, Brandés S, Sutter JP (2007) Nanoporous magnets of chiral and racemic [{Mn-(HL)}2Mn{Mo(CN)7}2] with switchable ordering temperatures (TC= 85K↔106 K) driven by H2O sorption (L = N, N-Dimethylalaninol). J Am Chem Soc 129:13872–13878. https://doi.org/10.1021/ja073612t

[48] Lehnert R, Seel F (1980) Darstellung und Kristallstruktur des Mangan(II)- und Zink(II)-Derivates des Imidazols. Z Anorg Allg Chem 464:187–194. https://doi.org/10.1002/zaac.19804640117

[49] Dyadkin V, Pattison Ph, Dmitriev V, Chernyshov D (2016) A new multipurpose diffractometer PILATUS@SNBL. J Synchrotron Radiat 23:825. https://doi.org/10.1107/S1600577516002411

[50] Favre-Nicolin V, Černý R (2002) FOX, "free objects for crystallography": a modular approach to ab initio structure determination from powder diffraction. J Appl Crystallogr 35:734–743. https://doi.org/10.1107/S0021889802015236

[51] Rodriguez-Carvajal J (1993) Recent advances in magnetic structure determination by neutron powder diffraction. Phys B 192:55–69. https://doi.org/10.1016/0921-4526(93)90108-I

[52] Rietveld HM (1969) A profile refinement method for nuclear and magnetic structures. J Appl Crystallogr 2:65–71. https://doi.org/10.1107/S0021889869006558

[53] Momma K, Izumi F (2011) VESTA 3 for three-dimensional visualization of crystal, volumetric and morphology data. J Appl Crystallogr 44:1272–1276. https://doi.org/10.1107/S0021889811038970

[54] Macrae CF, Edgington PR, McCabe P, Pidcock E, Shields GP, Taylor R, Towler M, van de Streek J (2006) Mercury: visualization and analysis of crystal structures. J Appl Crystallogr 39:453–457. https://doi.org/10.1107/S002188980600731X

[55] Matěj Z, Kužel R, Nichtová L (2010) XRD total pattern fitting applied to study of microstructure of TiO$_2$ films. Powder Diffr 25:125–131. https://doi.org/10.1154/1.3392371

[56] Cliffe MJ, Goodwin AL (2012) PASCal: a principal-axis strain calculator for thermal expansion and compressibility determination. J Appl Cryst 45:1321–1329. https://doi.org/10.1107/S0021889812043026

[57] Černý R, Favre-Nicolin V (2007) Direct space methods of structure determination from powder diffraction principles, guidelines and perspectives. Z Kristallogr 222:105–113. https://doi.org/10.1524/zkri.2007.222.3-4.105

[58] Brese NE, O'Keeffe M, Bond-Valence Parameters for Solids (1991) Acta Crystallogr, Sect B: Struct Sci B47, 192−197, https://doi.org/10.1107/S0108768190011041

[59] Richter B, Ravnsbaek DB, Tumanov N, Filinchuk Y, Jensen TR (2015) Manganese borohydride; synthesis and characterization. Dalton Trans 44:3988–3996. https://doi.org/10.1039/C4DT03501A

[60] Černý R, Penin N, Hagemann H, Filinchuk Y (2009) The first crystallographic and spectroscopic characterization of a 3d-metal borohydride: Mn(BH$_4$)$_2$. J Phys Chem C 113:9003–9007. https://doi.org/10.1021/jp9015883

[61] Tumanov NA, Roedern E, Łodziana Z, Nielsen DB, Jensen TR, Talyzin AV, Černý R, Chernyshov D, Dmitriev V, Palasyuk T, Filinchuk Y (2016) High-pressure study of $Mn(BH_4)_2$ reveals a stable polymorph with high hydrogen density. Chem Mater 28:274–283. https://doi.org/10.1021/acs.chemmater.5b04102

[62] Shannon RD (1976) Revised effective ionic radii and systematic studies of interatomic distances in halides and chalcogenides. Acta Cryst A32:751–767. https://doi.org/10.1107/S0567739476001551

[63] Filinchuk Y, Chernyshov D, Černý R (2008) Lightest borohydride probed by synchrotron X-ray diffraction: experiment calls for a new theoretical revision. J Phys Chem C 112:10579–10584. https://doi.org/10.1021/jp8025623

[64] Korte C, Keppner J, Peters A, Schichtel N, Aydin H, Janek J (2014) Coherency strain and its effect on ionic conductivity and diffusion in solid electrolytes-an improved model for nanocrystalline thin films and a review of experimental data. Phys Chem Chem Phys 16:24575–24591. https://doi.org/10.1039/C4CP03055A

[65] Bhattacharyya A, Maurice D (2018) On the evolution of stresses due to lattice misfit at a Ni-superalloy and YSZ interface. Surf Interfaces 12:86–94. https://doi.org/10.1016/j.surfin.2018.05.007

Publisher's Note Springer Nature remains neutral with regard to jurisdictional claims in published maps and institutional affiliations.